A Facile Carbon Quantum Dot-Modified Reduction Approach Towards Tunable Sb@CQDs Nanoparticles for High Performance Sodium Storage

Fei Liu,[a] Yaping Wang,[a] Yifang Zhang,*[a] Jiande Lin,[a] Qiong Su,[a] Junrong Shi,[a] Xuefang Xie,[a] Shuquan Liang,[a] and Anqiang Pan*[a]

Antimony (Sb) has considerable specific capacity as an anode material for sodium-ion batteries. However, the large volume expansion during alloying/dealloying with Na^+ leads to poor cycling stability. Herein, we report the synthesis of Sb@carbon quantum dots (Sb@CQDs) composite via a facile one-step reduction approach at room temperature. CQDs can modify the nucleation and growth of Sb particles during the reduction process and thus tune the size of Sb. Sb@CQDs particles with size of ~7 nm can relieve the volume expansion and reduce the diffusion distance for sodium ions. Moreover, the residual CQDs in the obtained composite enhance the electronic conductivity. Benefited from the modification of CQDs, the Sb@CQDs composite delivers high specific capacity of 635 mAh g^{-1} at 0.1 A g^{-1} and 334 mAh g^{-1} at 2 A g^{-1}.

1. Introduction

Lithium-ion batteries (LIBs) have been the most promising energy storage devices for electric/hybrid electric vehicles and portable appliances over the past decades.[1,2] However, owing to the limited lithium resources, sodium-ion batteries (SIBs) have gained considerable attentions.[3] Nevertheless, the larger size of Na^+ than Li^+ plagues the kinetics of Na^+ chemistry in the host materials.[4,5] For example, commercial graphite exhibits low sodium storage capacity in carbonate electrolyte.[6,7] Hard carbon, based on the absorption-insertion Na^+ storage mechanism, shows higher capacity (~300 mAh g^{-1}) than graphite, but still suffers from low coulombic efficiency.[8–13]

Metal-based anodes (Sn, Ge, Sb, etc.) have been proposed for SIBs due to their high gravimetric/volumetric capacities.[3] Among all reported metallic anodes, antimony (Sb) processes high theoretical capacity (660 mAh g^{-1}), appropriate redox potential range (0.5–0.8 V vs Na^+/Na) and high electronic conductivity (2.56×10^6 S m^{-1}).[14,15] However, the significant volume expansion (up to 390%) and sluggish kinetics during the sodiation/desodiation process result in poor cycling stability. Nanostructured active materials can facilely release the stress and facilitate the transfer of Na^+.[16,17] However, the aggregation of nanoparticles during the cycling process limits the retainability of the electrochemical performance. In order to address this issue, researchers are devoted to fabricate composite structures with carbon or other conductive substrates supporting and dispersing the active nanoparticles. For example, a porous Sb/C composite prepared from alginate exhibited capacity of 380 mAh g^{-1} at 0.1 A g^{-1} after 200 cycles.[18] Sb@PCFs nanofibers prepared by electrospinning delivered reversible capacity of 538 mAh g^{-1} at 0.2 A g^{-1} after 80 cycles, much improved comparing with bulk Sb which showed quickly decayed capacity within the initial 5 cycles.[19] Despite the improvement made by carbon, the overall capacity of electrode could be compromised by constructing an integrated substrate, which needs the carbon content to reach an adequate level. It is thus desirable to develop other synthetic approaches and compositing forms to disperse active nanoparticles with low carbon content.

Carbon quantum dots (CQDs) are nano-scaled carbon materials with diameters of below 10 nm, which are extensively used in drug delivery, bioimaging, photocatalysis and chemical sensing.[20,21] CQDs with various surface passivation structures can effectively induce the growth of crystals, which as a "designer additive" can modify the morphology and surface structure of composite materials.[20] For example, CQDs tuned the morphology of Mn_3O_4 from irregular particles to octahedra[22] and induced the growth of TiO_2 to form a petal-like structure.[23] Recently, a lot of research works suggest that CQDs exhibit superior performances as conductive additives in electrochemical energy storage. As electrode materials for supercapacitors, RuO_2 modified by CQDs displayed a high specific capacitance of 460 F g^{-1} at a current density of 50 A g^{-1}.[24] As anode materials for LIBs, Nb_2O_5/CQDs nanocomposites delivered a capacity of 385 mAh g^{-1} after 100 cycles at 0.1 A g^{-1}.[21] The compositing of active materials with CQDs to obtain specific structure and property is thus considered to be an interesting subject to develop new electrode materials for SIBs.

Here we report a homogeneous Sb@CQDs composite prepared via one-step reduction of $SbCl_3$ using CQDs as disperser and sodium borohydride as reductive agent. CQDs as

[a] F. Liu, Y. Wang, Y. Zhang, J. Lin, Q. Su, J. Shi, X. Xie, S. Liang, Dr. A. Pan
School of Materials Science & Engineering
Central South University
Changsha, Hunan, 410083, P.R. China
E-mail: zhangyifang@csu.edu.cn
pananqiang@csu.edu.cn

effective functionalized inducer can tune the size of Sb particles in the synthetic process. The obtained Sb@CQDs nanocomposite is favorable for shortening the diffusion distance of Na^+, buffering the volume changes and enhancing the electronic conductivity, which optimizes the electrochemical properties of Sb-based material as anode for SIBs. Compared with bulk Sb particles, the Sb@CQDs composite electrodes display excellent electrochemical performance, including highly reversible capacity of 635 mAh g^{-1} at 0.1 A g^{-1} and remarkable rate capability (334 mAh g^{-1} at 2 A g^{-1}).

Experimental Section

Materials synthesis

Preparation of CQDs

The CQDs were conveniently synthesized by anodic oxidation of alcohol according to previous literature.[25] In a typical synthesis, a mixture consisting of 1 g of NaOH, 10 mL of water and 140 mL of alcohol was used as electrolyte solution. Two Pt sheets (15× 15 mm^2) were applied as the working and counter electrodes, respectively, with static potential of 20 V employed to them. Dark brown solution containing CQDs was obtained after electrolysis for 24 h. Subsequently, 150 mL of ethanol was added to the mixture solution to salt out the NaOH and the supernatant was dialyzed for 24 h to remove residual NaOH. Then the CQDs powders were obtained by drying in an oven at 60 °C.

Preparation of Sb@CQDs

0.8 g of SbCl$_3$ was dissolved in 50 mL of ethanol. 0.4 g of NaBH$_4$ reductive agent was dissolved in another 50 mL of ethanol. To study the effect of CQDs on the synthetic process of Sb, high dose (0.2 g), low dose (0.1 g) or no CQDs powders were added in the NaBH$_4$ solution, followed by sonication for 0.5 h. The SbCl$_3$ solution was added to the above mentioned mixture, which was allowed to react for 3 h. Sb@CQDs composite or pure Sb was harvested by centrifugation, washed with water and ethanol for three times, respectively, and dried in an oven at 60 °C. The samples obtained with high dose, low dose and without CQDs were denoted as Sb@CQDs-H, Sb@CQDs-L and Sb, respectively.

Materials characterization

The crystallography of the obtained products was determined by power X-ray diffraction (XRD, Rigaku D/max 2500, Cu K$_\alpha$ radiation, $\lambda = 1.54178$ Å). Nitrogen adsorption-desorption measurements were conducted by Micromeritics ASAP 2460. The thermogravimetric analysis (TGA) and differential scanning calorimetry (DSC) (NETZSCH STA 499C) were performed under air atmosphere from 25 to 800 °C at a ramping rate of 10 °C min^{-1}. The morphologies and sizes of the as-obtained products were characterized by scanning electron microscopy (SEM, Quanta FEG 250) and transmission electron microscope (TEM, JEOL JEM-2100F). X-ray photoelectron spectroscopy (XPS) measurements were conducted on an ESCALAB 250 Xi (ThermoFisher-VG Scientific, Britain).

Electrochemical characterization

Active materials were mixed with Super P and sodium carboxymethyl cellulose (CMC) in a mass ratio of 70:15:15 in deionized water to form a slurry, which was coated on Cu foil. The active materials are the Sb@CQDs-H, Sb@CQDs-L and Sb, respectively, and the electrochemical performance is evaluated on the total masses of Sb@CQDs-H and Sb@CQDs-L. 1 M NaClO$_4$ in propylene carbonate (PC) with 5 % (in volume) fluorinated ethylene carbonate (FEC) and glass microfiber filters (Whatman GF/D) were employed as electrolyte and separator, respectively. The electrochemical performances of the as-prepared electrodes for SIBs were tested using CR2016-type coin cells with sodium foil as the counter and reference electrode. Cyclic voltammetry (CV) tests (0.01–2.0 V vs Na/Na$^+$) were conducted on a CHI660E (Shanghai Chenhua) electrochemical workstation. All the galvanostatic charge/discharge tests of the as-assembled batteries were performed with a Land Battery Tester (Land CT2001 A, China) in the voltage range of 0.01– 2.0 V (vs Na/Na$^+$). EIS (from 100 kHz to 10 mHz) was performed on electrochemical workstation (MULTI AUTOLOABM204, Metrohm).

2. Results and Discussion

Figure 1 illustrates the formation process of the as-prepared Sb and Sb@CQDs samples to depict the CQDs-induced growth mechanism. Sb^{3+} can be effectively reduced by NaBH$_4$ and grow into antimony crystal. The pure crystals are large particles, which lead to large volume expansion during alloying/dealloying progress. With the modification of CQDs, small and uniform Sb@CQDs nanoparticles can be produced. The CQDs are identified as structure designers, which can induce the homogeneous nucleation and growth of Sb particles during the preparation process. The Sb particles are surrounded by CQDs to alleviate the fragmentation caused by volume expansion, and the CQDs can also serve as electronic conductive channels. It is worth mentioning that, when a low dose of CQDs is employed, the obtained Sb@CQDs-L composite possess much reduced particle size, as the dose of CQDs increases to a higher level, the particle size of Sb@CQDs-H can be further decreased. The controllable synthesis of Sb@CQDs with tunable particle size is thus realized by the modification of CQDs. Moreover, the introduction of CQDs facilitates the structural stability and conductivity of the composite, which as electrode materials for SIBs can contribute positive effect on the electrochemical performance.

The morphologies of the Sb-based reduction products are characterized by SEM and TEM. The SEM image Figure 2a shows the Sb sample without the modification of CQDs is composed of micron-sized blocks with size of ∼3 μm. The particle size of Sb can be largely reduced after introducing CQDs in the reduction process. The TEM image of CQDs is presented in Figure S1, which presents an average size of 3 nm. The Sb@CQDs-L composite is uniform particles with size of ∼1 μm (Figure 2b). The size of Sb can be further reduced by employing a higher dose of CQDs in the reaction solution (Figure 2c). The TEM image (Figure 2d) of the Sb@CQDs-H composite presents that the nanoparticles are with diameter of approximately 7 nm. Figure 2e depicts the HRTEM image of the Sb nanoparticles decorated with CQDs and shows the lattice fringes of
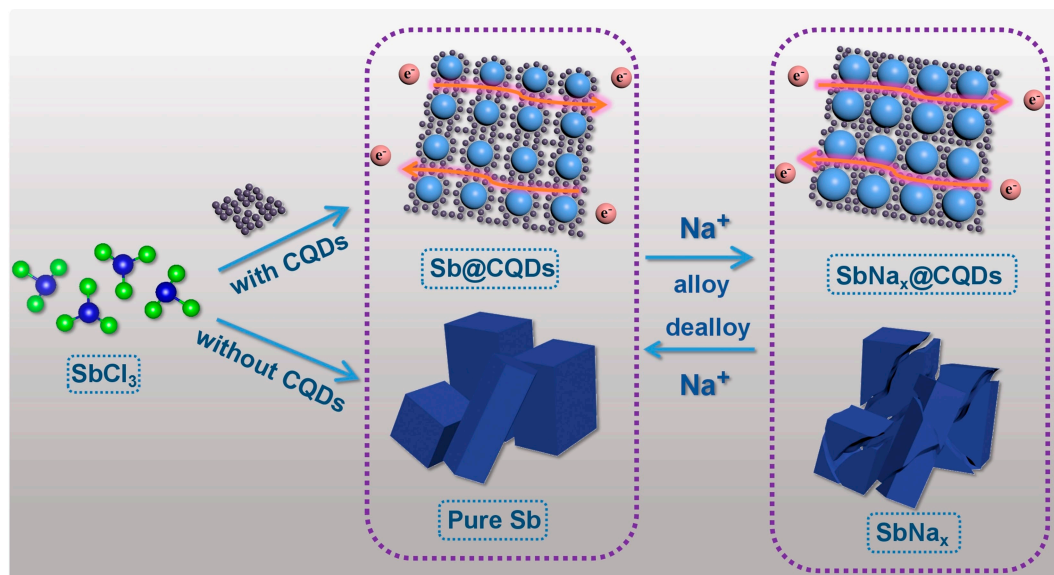
Figure 1. Schematic illustration of the formation process of pure Sb and Sb@CQDs composites.
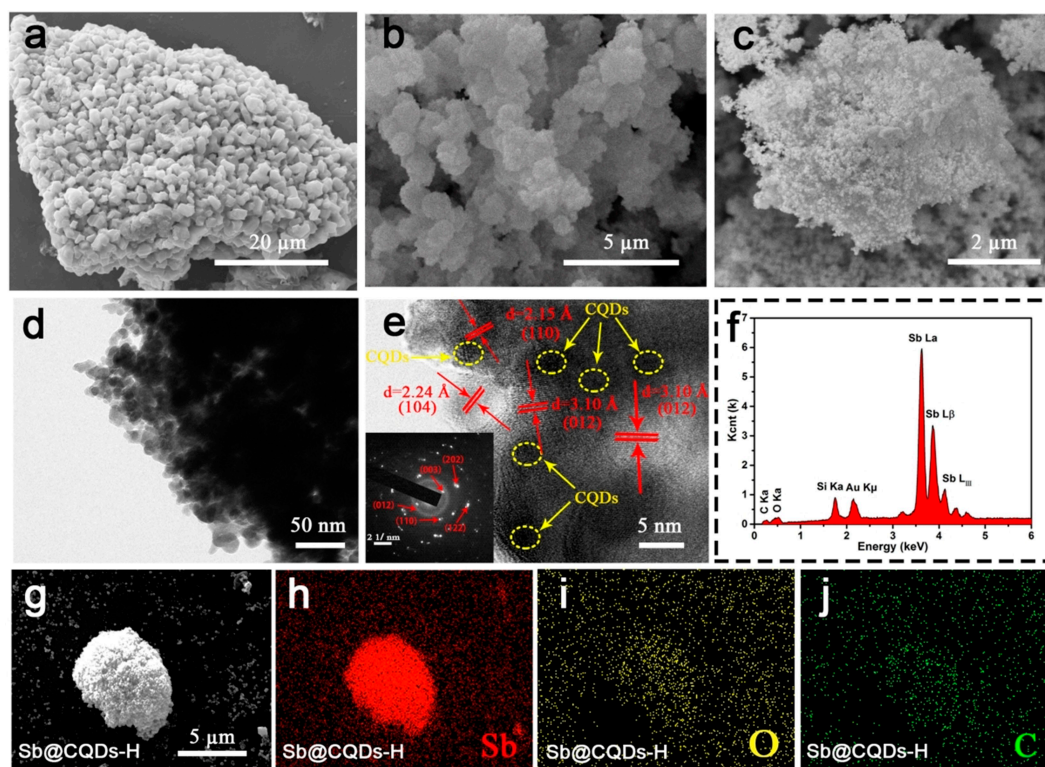

Figure 2. SEM images of (a) Sb, (b) Sb@CQDs-L and (c) Sb@CQDs-H. (d) TEM image, (e) HR-TEM image, (f) EDS pattern and (g-j) elemental mapping of Sb@CQDs-H.

2.15, 2.24, and 3.10 Å, which are corresponding to the (110), (104), and (012) planes of Sb, respectively. In the inset of Figure 2e, the selected-area electron diffraction (SAED) patterns indicate the polycrystalline feature of the Sb@CQDs-H sample, and show relatively obvious diffraction rings corresponding to the (003), (012), (110), (202), and (122) crystalline planes, which are consistent with the XRD results. SEM-EDS spectra and

elemental mapping results (Figure 2f–j) indicate the homogeneous distribution of Sb, O, and C for the Sb@CQDs-H composite.

The phases of Sb@CQDs-H, Sb@CQDs-L and Sb samples were analyzed by XRD. As shown in Figure 3a, all the diffraction peaks of the three samples can be well-indexed to trigonal Sb (JCPDS No. 83-1322), indicating Sb^{3+} was reduced to Sb by

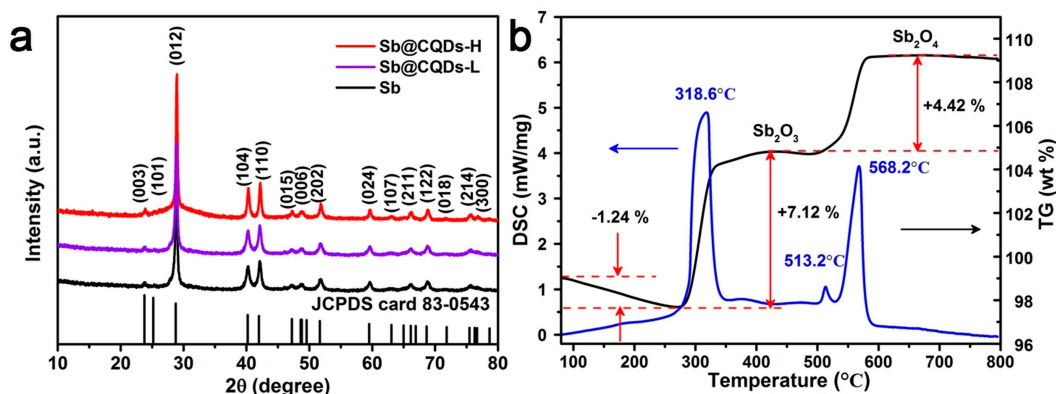**Figure 3.** (a) XRD patterns of Sb@CQDs-H, Sb@CQDs-L and Sb. (b) TGA and DSC curves of Sb@CQDs-H in air.

NaBH$_4$. TGA and DSC were performed to estimate the carbon content of Sb@CQDs, which were operated from room temperature to 800 °C in air at a heating rate of 10 °C min^{-1}. The curves are presented in Figure 3b, with the weight of the composite increasing at about 318.6 °C and 568.2 °C, which may result from the oxidation reactions of Sb to Sb$_2$O$_3$ and then to Sb$_2$O$_4$.[26] The exothermal peak at 513.2 °C and the weight decrease can be ascribed to the burning of CQDs.[22] Based on the reaction mechanism, the carbon content in Sb@CQDs-H can be deduced to be 12.54 wt.%.

The XPS survey spectrum of Sb@CQDs-H is shown in Figure 4a, which indicates the existence of Sb, C and O elements. As shown in Figure 4b, the C 1s spectrum can be deconvoluted into four peaks, which can be identified as sp3 hybridized (C—C, 284.6 eV), alcoholic (C—OH, 284.9 eV), carbonyl (C═O, 286.1 eV), and carboxyl (O—C═O, 288.4 eV) carbon atoms, respectively.[27] Figure 4c shows the high-resolution XPS spectrum of Sb 3d. The binding energies at

530.3 and 539.7 eV correspond to the Sb 3d$_{5/2}$ and Sb 3d$_{3/2}$ of Sb^{3+}. While the binding energies at 528.0 and 537.4 eV correspond to the Sb 3d$_{5/2}$ and Sb 3d$_{3/2}$ of Sb^0. The peak at 530.9 eV can be assigned to O 1s which shifts slightly to higher binding energy owing to the existence of Sb—O—C bond.[28]

As depicted in Figure 5a and **5b**, the N$_2$ adsorption-desorption isotherm of Sb@CQDs-H and Sb@CQDs-L show a character of type IV isotherm with type H3 hysteresis loop.[29] The BET surface area is 37.036 m^2 g^{-1} and 7.9627 m^2 g^{-1} respectively. The pore size distribution curve shows that the Sb@CQDs–H sample has a wide range of micro/mesopores distributed from 2 to 30 nm, and the Sb@CQDs-L sample has a wide range of micro/mesopores distributed from 2 to 5 nm. In contrast, the N$_2$ adsorption-desorption isotherm and pore size distribution of pure Sb shown in Figure 5c only deliver a BET surface area of 7.9627 m^2 g^{-1}. The higher surface area of Sb@CQDs-H and Sb@CQDs-L composite can be attributed to the modification of CQDs that tunes the size of Sb particles and
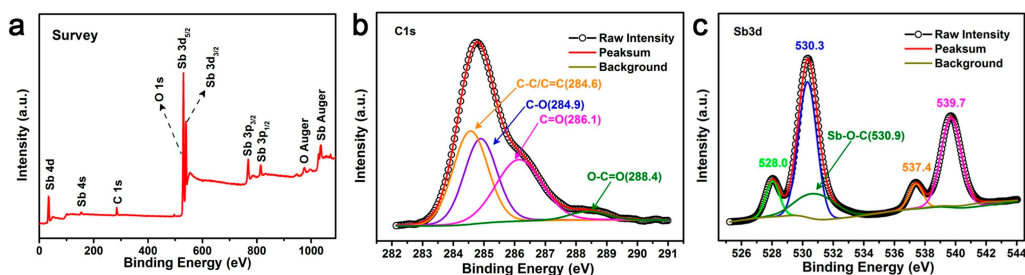

Figure 4. (a) XPS survey spectrum of Sb@CQDs-H. High-resolution XPS spectra of (b) C 1s and (c) Sb 3d of Sb@CQDs-H composite.
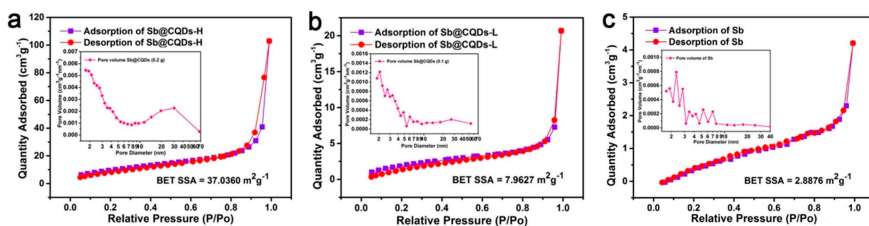

Figure 5. Nitrogen adsorption/desorption curves and pore-size distribution curves (insets) of (a) Sb@CQDs-H, (b) Sb@CQDs-L and (c).

effectively prevents the aggregation. The larger surface area can enlarge electrode-electrolyte contact area and accelerate the mass transfer.

The electrochemical performances of the as-obtained Sb@CQDs-H composite were measured by sodium half-cells. As shown in Figure 6a, the initial three CV curves of Sb@CQDs-H were carried out at a scanning rate of 0.1 mVs^{-1} in the potential range of 0.01–2 V vs Na/Na$^+$. The reduction peaks at 0.68, 0.46 and 0.25 V during the first cathodic scan can be attributed to the multistep alloying reaction from Sb to NaSb and then to Na$_3$Sb, along with the decomposition of electrolyte and the formation of solid-electrolyte interface (SEI) film.[30,31] In the anodic scan, the broad peak appeared at 0.11 V can be ascribed to the dealloying reaction of Na$^+$ extracted from Na$_x$Sb ($x \leq 3$). The CV curve of the third cycle is similar to the second one, indicating the improved reversibility of the Sb@CQDs-H electrode. Figure 6b displays the charge/discharge curves of the Sb@CQDs-H composites at a current density of 0.1 A g^{-1}. The charge-discharge plateaus are in good accordance with the anodic/cathodic peaks in the CV curves. The initial discharge and charge capacities for Sb@CQDs-H are 733 and 584 mA h g^{-1}, respectively, with an initial Coulombic efficiency of 79.65%. The irreversible capacity can be ascribed to the formation of SEI film and the incomplete extraction of sodium from the active composites, which is also testified by CV analysis.

Figure 6c shows the cyclic performances of Sb@CQDs-H, Sb@CQDs-L and Sb electrodes at current density of 0.1 A g^{-1}. For the Sb@CQDs-H composite electrode, a reversible capacity of 587 mA h g^{-1} can be retained after 120 cycles. In contrast, the Sb@CQDs-L shows poor cycling stability and the pure Sb sample exhibits much lower capacity. The Sb materials are larger in particle size for Sb@CQDs-L, which are less resistible to the volume changes during the repeated sodiation/desodiation process, leading to rapidly decreased capacity. The sizes of pure Sb particles are even larger, which may limit the full release of capacity owing to the sluggish kinetics of Na alloying

reaction. The SEM images of the Sb@CQDs-H and Sb after 120 at 0.1 A g^{-1} are shown in Figure S2. Compared with the Sb, the Sb@CQDs-H presents smaller particles with less aggregation. Figure 6d exhibits the rate capacity of the electrodes. At increasing current densities of 0.1, 0.2, 0.5, 1 and 2 A g^{-1}, the Sb@CQDs-H composite delivers high specific capacity of 635, 614, 510, 439 and 334 mA h g^{-1}, respectively. The reversible capacity of 633 mA h g^{-1} can be resumed when resetting the current to 0.1 A g^{-1}. For the Sb@CQDs-L sample, although relatively high capacity can be obtained at low current densities, only 264 mA h g^{-1} of capacity can be released at 0.5 A g^{-1}. As the current is reset to 0.1 A g^{-1}, the capacity cannot be recovered. While for the pure Sb sample, the capacity is low at all current densities. In Figure 6e, the cycling performance of Sb@CQDs-H composite electrode at a current density of 0.5 A g^{-1} shows that a reversible capacity of 510 mA h g^{-1} can be retained after 120 cycles, which displays much better cycling stability than Sb@CQDs-L and Sb electrodes.

A comparison on electrochemical performances of this work and recently reported Sb-based anode materials for SIBs is shown in Table 1. The as-synthesized Sb@CQDs-H composite delivers higher electrochemical performances than those of previous studies, in terms of both rate capability and cycling stability.

To elucidate the chemical diffusion coefficient and conductivity properties of Sb@CQDs-H and Sb, GITT tests were performed.[37,38] The sodium diffusion coefficients (D_{Na}^+) at different discharge/charge voltages were calculated according to Equation S1, and the results of the first two cycles are shown in Figure 7. The D_{Na}^+ of the Sb@CQDs-H composite is higher than that of pure Sb at most sodiation/desodiation states, which is mainly attributed to that the Sb@CQDs-H nanoparticles possess larger electrode/electrolyte contact area for sodium diffusion. Furthermore, the composites with CQDs have more favorable active sites compared with pure Sb. The D_{Na}^+ of Sb is close to Sb@CQDs-H at the first discharge curve. However, in the subsequent curves, the D_{Na}^+ of Sb decrease rapidly
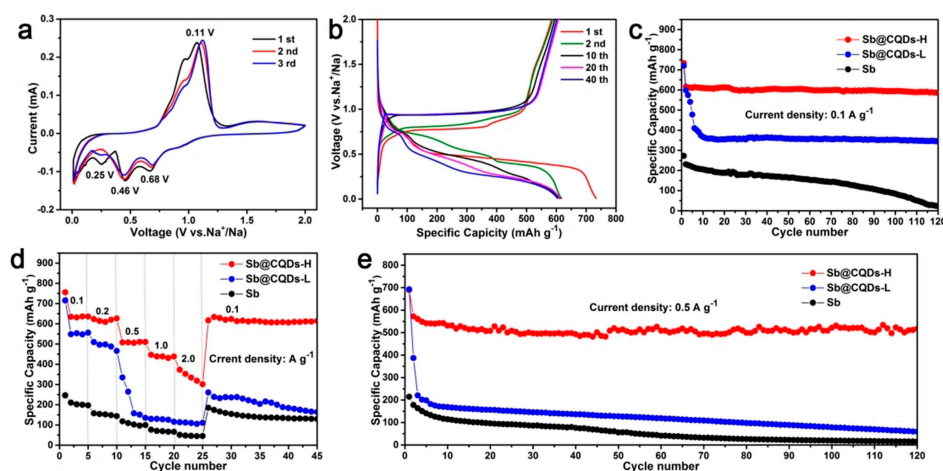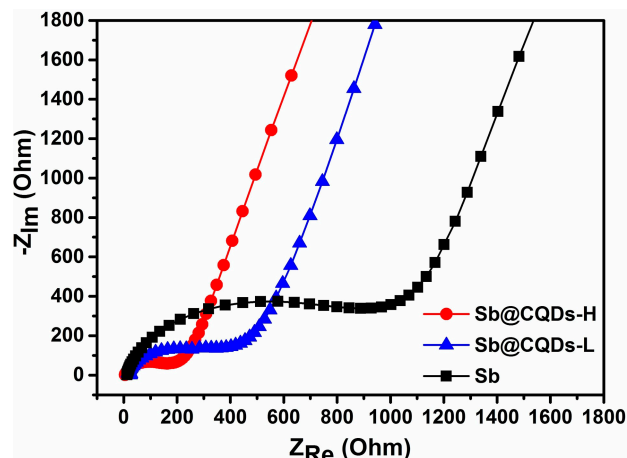

Figure 6. (a) CV curves of Sb@CQDs-H at scan rate of 0.1 mVs^{-1}. (b) Selected galvanostatic charge-discharge curves of Sb@CQDs-H at current density of 0.1 A g^{-1}. (c) Cycle performances at 0.1 A g^{-1}, (d) rate performances at different current densities from 0.1 to 2 A g^{-1}, and (e) cycle performances at 0.5 A g^{-1} of Sb@CQDs-H, Sb@CQDs-L and Sb.

Table 1. Comparison of several Sb-based anode for sodium-ion batteries

Electrode material	Rate capability	Capacity retention	Ref.
Sb/graphene	415 (2 A g^{-1}) and 220 mAh g^{-1} (12 A g^{-1})	460 mAh g^{-1} (0.25 A g^{-1}), 200 cycles	[32]
Nanoporous Sb	510 (1.32 A g^{-1}) and 420 mAh g^{-1} (3.3 A g^{-1})	574 mAh g^{-1} (0.1 A g^{-1}), 200 cycles	[33]
Sb@C yolk-shell	554 (50 mA g^{-1}) and 315 mAh g^{-1} (5 A g^{-1})	92 % (500 mA g^{-1}), 200 cycles	[34]
Sb/N-doped porous carbon	561 (0.1 A g^{-1}) and 287 mAh g^{-1} (3.2 A g^{-1})	97 % (0.1 A g^{-1}), 100 cycles	[35]
Sb/C nanocomposite	420 (0.25 A g^{-1}) and 138 mAh g^{-1} (32 A g^{-1})	94 % (0.5 A g^{-1}), 100 cycles	[36]
Sb@PCF	385 (1.5 A g^{-1})	96 % (0.2 A g^{-1}), 80 cycles	[19]
Carbon nanofibers networks/Sb	552 (0.1 A g^{-1}) and 315 mAh g^{-1} (3.2 A g^{-1})	96.7 % (0.1 A g^{-1}), 100 cycles	[26]
Sb@CQDs-H	633 (0.1 A g^{-1}) and 334 mAh g^{-1} (2 A g^{-1})	587 mAh g^{-1} (0.1 A g^{-1}), 120 cycles	This work

Figure 8. Electrochemical impedance spectroscopy of Sb@CQDs-H, Sb@CQDs-L and Sb electrodes.

owing to crushing structure, which is attributed to volume expansion of Sb at the first discharge curve. The minimums of D_{Na^+} appear at the plateaus of charge/discharge curves. In the first discharge curve, two local minimal points can be observed for the Sb@CQDs-H electrode (marked with red circles), indicating the multistep alloying reactions (Sb to NaSb and NaSb to Na$_3$Sb) are taking place at the corresponding voltages (Figure 7 and Figure S4). For the pure Sb sample, only one minimal point appears, indicating the active materials may experience more severe alloying reactions (Sb to Na$_3$Sb) at lower voltage (Figure S4). The different kinetic characters of the two electrodes imply the nanostructured Sb@CQDs-H composites are favorable for enhancing the capacity owing to the large electrode/electrolyte contact area and short Na$^+$ transfer path.

The EIS results shown in Figure 8 indicates that the charge transfer resistance of Sb@CQDs-H composite in SIBs is 200 Ω, which is about two times lower than that of Sb@CQDs-L (ca. 400 Ω) and five times lower than that of Sb (ca. 1000 Ω). Also, direct measurement of conductivity has been detected by Yang et al. demonstrating that the electrical conductivity of the

composite with CQDs is about ten times higher than that of pure sample, which can be ascribed to the decorating of CQDs. These results clearly indicate that the CQDs improve the electrical conductivity and charge transfer reactions.[34]

3. Conclusions

In summary, a novel homogeneous Sb@CQDs composite was successfully synthesized via one-step reduction route. CQDs as functionalized inducers can effectively tune the size and prevent the aggregation of Sb particles. Sb@CQDs-H nanoparticles exhibit high specific capacity of 635 and 510 mAh g^{-1} at current densities of 0.1 and 0.5 A g^{-1} for SIBs. The remarkable electrochemical performances can be ascribed to the unique structure modified by CQDs, which can enlarge the contact area of electrode and electrolyte, shorten the Na$^+$ transfer path, and alleviate the volume changes along cycling.
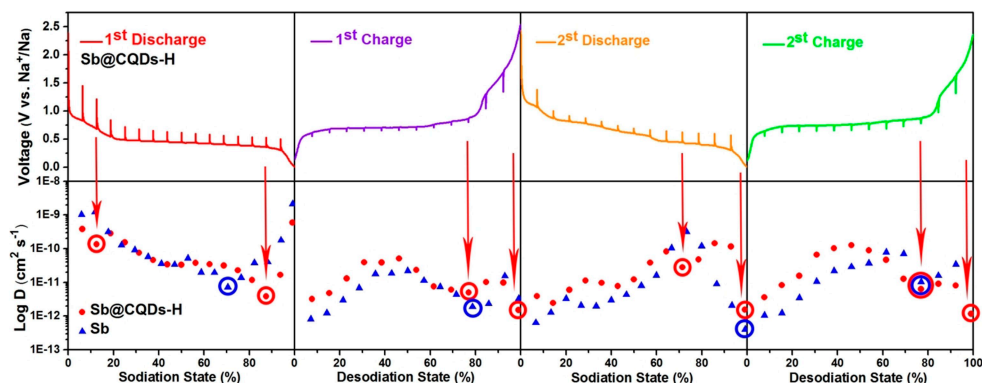
Figure 7. GITT curves and the corresponding Na$^+$ diffusion coefficient at different discharge/charge states of Sb@CQDs-H and Sb electrodes.

Batteries & Supercaps

Articles
doi.org/10.1002/batt.201900167

Chemistry Europe
European Chemical
Societies Publishing

Acknowledgments

Conflict of Interest

The authors declare no conflict of interest.

[1] A. Magasinski, P. Dixon, B. Hertzberg, A. Kvit, J. Ayala, G. Yushin, *Nat. Mater.* **2010**, *9*, 353–358.

[2] Y. Wang, Z. Nie, A. Pan, Y. Zhang, X. Kong, T. Zhu, S. Liang, G. Cao, J. Mater, *Chem. Chron. A* **2018**, *6*, 6792–6799.

[3] Y. Wang, Y. Zhang, J. Shi, A. Pan, F. Jiang, S. Liang, G. Cao, J. Mater, *Chem. Chron. A* **2018**, *6*, 18286–18292.

[4] S. P. Ong, V. L. Chevrier, G. Hautier, A. Jain, C. Moore, S. Kim, X. Ma, G. Ceder, *Energy Environ. Sci.* **2011**, *4*, 3680–3688.

[5] Q. Su, X. Cao, X. Kong, Y. Wang, C. Peng, J. Chen, B. Yin, J. Shi, S. Liang, A. Pan, *Electrochim. Acta* **2018**, *292*, 339–346.

[6] P. Ge, M. Fouletier, *Solid State Ionics* **1988**, *28–30*, 1172–1175.

[7] Y. Zhang, Q. Su, W. Xu, G. Cao, Y. Wang, A. Pan, S. Liang, *Adv. Sci.* **2019**, *6*, 1900162.

[8] P. Li, J. Y. Jeong, B. Jin, K. Zhang, J. H. Park, *Adv. Energy Mater.* **2018**, *8*, 1703300.

[9] Y. Lin, Z. Qiu, D. Li, S. Ullah, Y. Hai, H. Xin, W. Liao, B. Yang, H. Fan, J. Xu, C. Zhu, *Energy Storage Mater.* **2018**, *11*, 67–74.

[10] X. Zhong, Y. Li, L. Zhang, J. Tang, X. Li, C. Liu, M. Shao, Z. Lu, H. Pan, B. Xu, *ACS Appl. Mater. Interfaces* **2019**, *11*, 2970–2977.

[11] Q. Wang, X. Zhu, Y. Liu, Y. Fang, X. Zhou, J. Bao, *Carbon* **2018**, *127*, 658–666.

[12] L. Li, Y. Zheng, S. Zhang, J. Yang, Z. Shao, Z. Guo, *Energy Environ. Sci.* **2018**, *11*, 2310–2340.

[13] F. Liu, Y. Wang, J. Shi, J. Lin, W. Zhou, A. Pan, *Electrochim. Acta* **2019**, *318*, 314–321.

[14] A. Darwiche, C. Marino, M. T. Sougrati, B. Fraisse, L. Stievano, L. Monconduit, J. Am, *Chem. Soc. Rev.* **2012**, *134*, 20805–20811.

[15] N. Zhang, Y. Liu, Y. Lu, X. Han, F. Cheng, J. Chen, *Nano Res.* **2015**, *8*, 3384–3393.

[16] N. Zhang, Q. Zhao, X. Han, J. Yang, J. Chen, *Nanoscale* **2014**, *6*, 2827–2832.

[17] L. Pei, Q. Jin, Z. Zhu, Q. Zhao, J. Liang, J. Chen, *Nano Res.* **2015**, *8*, 184–192.

[18] G. Wang, X. Xiong, Z. Lin, C. Yang, Z. Lin, M. Liu, *Electrochim. Acta* **2017**, *242*, 159–164.

[19] M. Zhu, X. Kong, H. Yang, T. Zhu, S. Liang, A. Pan, *Appl. Surf. Sci.* **2018**, *428*, 448–454.

[20] H. Hou, C. E. Banks, M. Jing, Y. Zhang, X. Ji, *Adv. Mater.* **2015**, *27*, 7861–7866.

[21] J. Lin, Y. Yuan, Q. Su, A. Pan, S. Dinesh, C. Peng, G. Cao, S. Liang, *Electrochim. Acta* **2018**, *292*, 63–71.

[22] M. Jing, J. Wang, H. Hou, Y. Yang, Y. Zhang, C. Pan, J. Chen, Y. Zhu, X. Ji, J. Mater, *Chem. Chron. A* **2015**, *3*, 16824–16830.

[23] Y. Zhang, C. W. Foster, C. E. Banks, L. Shao, H. Hou, G. Zou, J. Chen, Z. Huang, X. Ji, *Adv. Mater.* **2016**, *28*, 9391–9399.

[24] Y. R. Zhu, X. B. Ji, C. C. Pan, Q. Q. Sun, W. X. Song, L. B. Fang, Q. Y. Chen, C. E. Banks, *Energy Environ. Sci.* **2013**, *6*, 3665–3675.

[25] J. Deng, Q. Lu, N. Mi, H. Li, M. Liu, M. Xu, L. Tan, Q. Xie, Y. Zhang, S. Yao, *Chem. Eur. J.* **2014**, *20*, 4993–4999.

[26] H. Hou, M. Jing, Y. Yang, Y. Zhang, W. Song, X. Yang, J. Chen, Q. Chen, X. Ji, *J. Power Sources* **2015**, *284*, 227–235.

[27] X. Zhou, Z. Zhang, J. Wang, Q. Wang, G. Ma, Z. Lei, *J. Alloys Compd.* **2017**, *699*, 611–618.

[28] T. Wu, C. Zhang, H. Hou, P. Ge, G. Zou, W. Xu, S. Li, Z. Huang, T. Guo, M. Jing, X. Ji, *Adv. Funct. Mater.* **2018**, *28*, 1705744.

[29] M. Wang, X. Yu, L. Hou, A. Gagnoud, Y. Fautrelle, R. Moreau, X. Li, J. Energy, *Chem.* **2018**, *351*, 930–938.

[30] Y. Zhu, X. Han, Y. Xu, Y. Liu, S. Zheng, K. Xu, L. Hu, C. Wang, *ACS Nano* **2013**, *7*, 6378–6386.

[31] L. Wu, X. Hu, J. Qian, F. Pei, F. Wu, R. Mao, X. Ai, H. Yang, Y. Cao, *Energy Environ. Sci.* **2014**, *7*, 323–328.

[32] F. Wan, J. Guo, X. Zhang, J. Zhang, H. Sun, Q. Yan, D. Han, L. Niu, X. Wu, *ACS Appl. Mater. Interfaces* **2016**, *8*, 7790–7799.

[33] S. Liu, J. Feng, X. Bian, J. Liu, H. Xu, *Energy Environ. Sci.* **2016**, *9*, 1229–1236.

[34] J. Song, P. Yan, L. Luo, X. Qi, X. Rong, J. Zheng, B. Xiao, S. Feng, C. Wang, Y. Hu, Y. Lin, V. Sprenkle, X. Li, *Nano Energy* **2017**, *40*, 504–511.

[35] T. Wu, H. Hou, C. Zhang, P. Ge, Z. Huang, M. Jing, X. Qiu, X. Ji, *ACS Appl. Mater. Interfaces* **2017**, *9*, 26118–26125.

[36] J. Duan, W. Zhang, C. Wu, Q. Fan, W. Zhang, X. Hu, Y. Huang, *Nano Energy* **2015**, *16*, 479–487.

[37] G. Fang, Z. Wu, J. Zhou, C. Zhu, X. Cao, T. Lin, Y. Chen, C. Wang, A. Pan, S. Liang, *Adv. Energy Mater.* **2018**, 1703155.

[38] B. Yin, X. Cao, A. Pan, Z. Luo, S. Dinesh, J. Lin, Y. Tang, S. Liang, G. Cao, *Adv. Sci.* **2018**, *5*, 1800829.

[39] Y. Yang, X. Ji, J. Ming, H. Hou, Y. Zhu, L. Fang, X. Yang, Q. Chen, C. Banks, J. Mater, *Chem. Chron. A* **2015**, *3*, 5648–5655.